Coupling field simulation of soft capacitive sensors towards soft robot perception

Coupling field simulation of soft capacitive sensors towards soft robot perception

Delin Hu, *Student Member, IEEE*, Haotian Li, Francesco Giorgio-Serchi,*Member, IEEE* and Yunjie Yang, *Member, IEEE*

***Abstract*— Simulation is a standard tool for robot design, control and performance analysis. Numerous mature, thoroughly validated methods exist to build fast and reliable simulation models for traditional rigid robotics platforms. However, when it comes to novel soft robotics systems, most existing models concern themselves with the dynamics of the soft bodies during actuation, largely disregarding the sensory system. Simultaneous simulation of sensors and actuators is essential to establishing a realistic and accurate robot model in the virtual environment. This paper proposes a pipeline to implement Coupling Field Simulation (CFS) of capacitive sensors deployed on a square soft arm and a pneumatic manipulator. The CFS approach can seamlessly integrate mechanical and sensing components, enabling us to understand sensor behaviour better by simulating sensor responses to various deformations including bending, inflation and the combinations of bending, twisting and elongation. We also demonstrate CFS is an effective and costly manner to acquire a large number of annotated data that can be used for pre-training in soft robot perception tasks through two case studies (i.e., applied force estimation and deformation classification).**

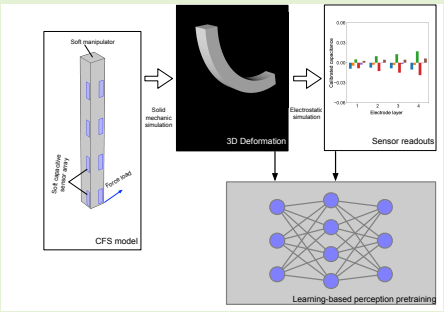

***Index Terms*— Coupling field simulation, soft capacitive sensor array, soft robots**

I. Introduction

In the past decades, robotics applications have become ubiquitous, spreading widely across fields that range from large-scale industrial manufacturing [1] to search and rescue in hazardous environments [2] and relieving human operators from heavy physical labour and unsafe working conditions. The rigid mechanical nature that guarantees accurate discrete kinematics is essential to the aforementioned success. However, as robots become more deeply involved with humans' activities, this property limits their flexibility and manoeuvrability. It poses potential safety risks to users, preventing their adoption in crucial applications such as biomedicine and human-robot interaction [3]. The emergence of soft robots promises to address this major limitation of traditional systems by exploiting their own bodily compliance and therefore enabling them to interact with users and environments in a more lifelike, effective and safer manner [4].

In order to achieve closed-loop control and autonomy, robots are required to possess perception ability, providing sensory feedback for both geometric variations of their bodies and other external stimuli (e.g., physical contact). Perception of soft robots remains challenging as the high deformability not only places new challenges to sensor design, fabrication and deployment but also dramatically increases the complexity of sensing data analysis. Coupling field simulation (CFS) which combines mechanical and sensing components can play a critical role in developing perception systems in soft robots. The benefits include the following aspects.

- The feasibility of proposed perception methods can be verified in a fast and cost-effective manner through CFS compared with implementing experiments on physical platforms.
- The response of proposed sensors on various soft robots with different deformations and external stimuli can be characterized using CFS, which assists to understand sensor behaviour, quantitatively evaluate sensor performance and optimize sensor design.
- Deep learning approaches are frequently employed to interpret sensing data to target parameters (e.g. deformation class, applied force and coordinates of the end-effector) due to the difficulty of mathematically modelling the behaviour of soft sensors and robots. It normally requires a large number of labelled data as training samples to optimize network parameters. However, data annotation is extremely time and labour-consuming. Applying data generated by CFS to pre-train the network can significantly reduce the burden of data acquisition.

However, to our knowledge, most existing simulation models only concern themselves with the dynamics, morphology

This work is partly supported by the Data Driven Innovation Chancellor's Fellowship, the Wellcome Trust iTPA fund and the MRC Impact Acceleration Account.

D.H, H.L. and Y.Y. are with the Institute for Digital Communications, School of Engineering, The University of Edinburgh, Edinburgh, UK (e-mail: delin.hu@ed.ac.uk; AspirantKid@gmail.com, y.yang@ed.ac.uk).

F.G. is with the Institute for Integrated Micro and Nano Systems, School of Engineering, The University of Edinburgh, Edinburgh, UK (e-mail: F.Giorgio-Serchi@ed.ac.uk).

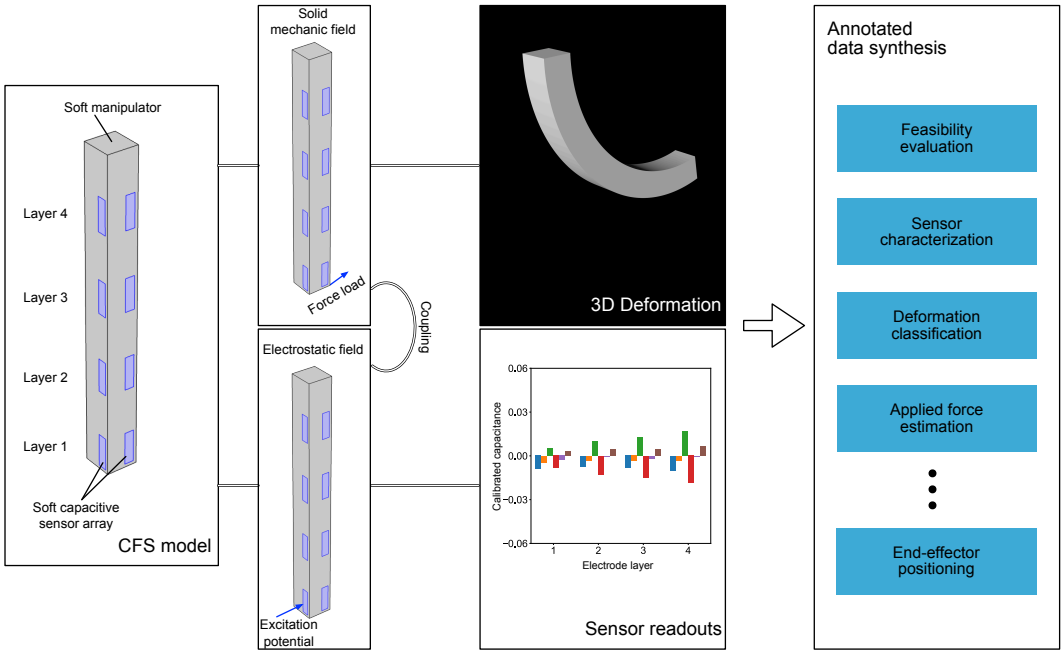

Fig. 1. Flowchart of Coupling Field Simulation (CFS) of a 16-electrode soft capacitive sensor array deployed on a square soft arm.

and actuation of soft robots, largely neglecting the sensory systems embedded in the mechanical structure [5]–[11]. For example, in [6], Finite Element Method (FEM) is employed to simulate the deformations of soft robots and their surroundings, which then helps achieve locomotion and manipulation for physical soft robots. Model Order Reduction [12] can simplify the computation of FEM-based simulations through snapshot-proper orthogonal decomposition, thus allowing a real-time simulation of soft robots with higher complexity. [9] explores shapes and gaits that adapt to different environments for a soft robot using simulation and successfully transfers the result to a physical platform. [10] attempts to optimize geometric configurations of soft locomotion robots in simulated environments via evolutionary algorithms. Recently, soft sensor design and placement optimization using simulation methods have been reported. In [11], a neural architecture for co-learning of general robotic tasks (e.g., tactile sensing and proprioception) and sensor placement is developed and demonstrated in a simulated environment. However, instead of simulating sensor behaviour under robot deformation and actuation, the study assumes the sensor has perfect performance (e.g., 100% accuracy, no latency, deployable to every location on the robot body), which is far from the practical conditions. Therefore, CFS methods which can combine sensing and mechanical components in soft robots and benefit the development of soft robot perception need to be investigated.

In this work, we propose CFS models for capacitive sensors deployed on two types of soft manipulators respectively (i.e., a square soft arm and a pneumatic soft actuator). The general framework of the proposed method is shown in Fig. 1. In the case of the square soft arm, solid mechanic field simulation is used to compute the deformation caused by a force load, while the sensor readouts corresponding to the deformation are obtained through electrostatic field simulation. The proposed CFS models can generate annotated data costly and effectively, benefiting the development loop for soft perception systems in many aspects as discussed above.

The contribution of this work is as follows.

- CFS models of a soft arm equipped with a 16-electrode capacitive sensor array and a pneumatic manipulator equipped with an 8-electrode capacitive sensor array are developed and implemented.
- The behaviours of sensors under various deformations including bending, the compound deformation of bending and twisting, the compound deformation of elongation and twisting and inflation are characterized and discussed.
- A large volume of annotated data is generated using the proposed method. Two neural architectures for different perception tasks (deformation classification and applied force estimation) are trained with the synthesis data. The trained networks can be used as per-trained models for real-world scenarios to reduce the burden of collecting data on physical platforms.

II. METHODOLOGY

This section introduces the fundamental principles of capacitive sensor arrays and CFS, with a focus on the coupling between solid mechanic, electrostatic, and fluid mechanic fields.

A. Capacitive sensor array

A planar capacitive sensor array consisting of several electrodes (e.g., 8 or 12) deployed on the outer surface of the Region Of Interest (ROI) can record the capacitance formed by different electrode combinations. In the non-deformable setup,

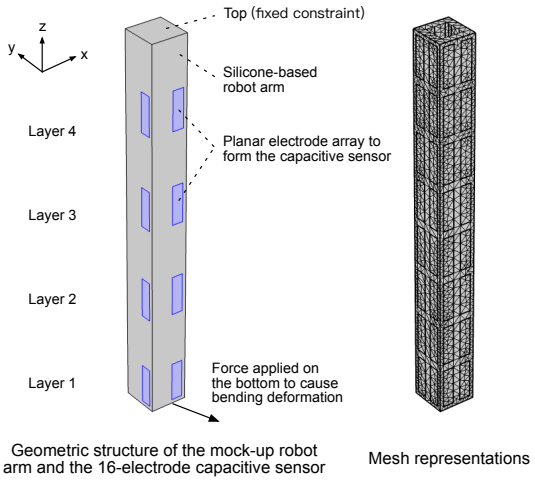

Fig. 2. Schematic illustration of the soft robot arm. Note that the other 8 electrodes are deployed on the two hidden surfaces.

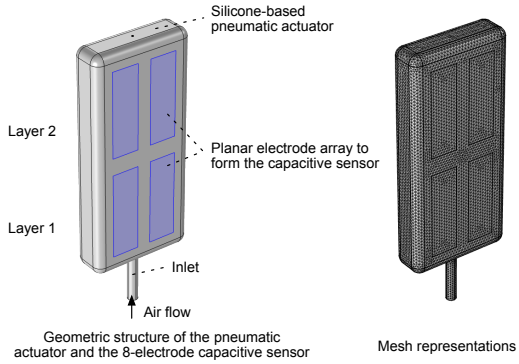

Fig. 3. Schematic illustration of the pneumatic actuator. Note that the other 4 electrodes are deployed on the hidden surface.

the permittivity distribution within the ROI can be inferred through the capacitance measurements by solving a dedicated inverse problem [13]. This technique is known as electrical capacitance tomography (ECT) and is frequently applied in industrial processes to non-invasively monitor the dynamic behaviours of multiphase flows. The relationship between the capacitance and its influencing factors can be described as [13], [14]

$$C = \frac{Q}{V} = -\frac{1}{V}\iint_{\Gamma} \epsilon(x,y,z)\nabla\phi(x,y,z)d\Gamma \tag{1}$$

where V is the potential difference between two electrodes that constitute the capacitor; $\epsilon(x,y,z)$ denotes the permittivity distribution in the ROI; $\phi(x,y,z)$ represents the potential distribution and Γ is the area of the electrode surface.

Conventional ECT utilizes rigid electrodes and aims to reconstruct the permittivity distribution based on a series of capacitance measurements. Here we consider capacitive sensor arrays made of soft materials. In this case, the capacitance is not only determined by the electrical properties of the internal medium, but also affected by the geometries of the objects under investigation. Notably, the two target manipulators have a constant permittivity while their 3D domain deforms. Therefore, the capacitance variation primarily reflects the geometric variation in the proximity of the electrode pair, enabling to infer the boundary deformation through capacitance readouts.

In the case of parallel plate capacitors with homogeneous material inside, the determining equation for capacitance can be simplified to

$$C = \epsilon_0\epsilon_r\frac{S}{l} \tag{2}$$

where ϵ_0 is the permittivity of vacuum; ϵ_r is the relative permittivity of the filling material; S is the area of the electrode and l is the distance between two electrodes. The capacitance is then positively correlated with S and negatively correlated with l. This is an intuitive observation that can assist qualitative understanding of the sensor response to deformation in the latter section.

B. Dynamics of the mechanical component

We first couple the solid mechanic and electrostatic fields to simultaneously simulate the dynamic deformation and capacitive sensor response of the first manipulator (see Fig. 2). To simulate the deformation, an external force is exerted at the endpoint of the manipulator. The relationship between stress and strain of an elastomer can be characterized by Hooke's law [15]

$$\boldsymbol{\xi} = \frac{1+\nu}{E}\boldsymbol{\sigma} - \frac{\nu}{E}\mathrm{tr}(\sigma)\boldsymbol{I} \tag{3}$$

where $\boldsymbol{\xi}$ is the strain tensor; $\boldsymbol{\sigma}$ is the stress tensor; ν denotes the Poisson's ration; E is the Young's modulus; tr$(\cdot)$ represents trace operator and $\boldsymbol{I}$ represents second-order identity tensor.

We use Eq. (3) to infer the deformation of the manipulator and then apply Eq. (1) to calculate capacitances formed by a series of electrode pairs following the conventional 3D ECT sensing protocol under the deformation.

For the pneumatic manipulator in Fig. 3, the fluid, mechanic and electrostatic fields are coupled to acquire deformations and capacitance measurements. In this case, the motion of the viscous fluid is governed by Navier-Stokes equations [16], [17]

$$\rho\frac{D\boldsymbol{u}}{Dt} = -\nabla p + \nabla\cdot\boldsymbol{\tau} + \rho\boldsymbol{g} \tag{4}$$

where ρ is the fluid density, $\boldsymbol{u}$ is the velocity vector, t is time, p is the pressure, $\boldsymbol{\tau}$ is the deviatoric stress tensor and $\boldsymbol{g}$ is the body accelerations. Hence, at quasi-static equilibrium the fluid-solid coupling occurs via $\boldsymbol{\sigma} \sim p\boldsymbol{\delta}$, with $\boldsymbol{\delta}$ being the Kronecker delta, thus enabling to relate driving pressure in Eq. (4) with body deformation in Eq. (3), and then solving Eq. (1) to obtain capacitance readouts.

III. Coupling Field Simulation

A. Case 1: soft robot arm

The first case involves a soft robot arm made of silicone (see Fig. 2 for the geometric structure). For computational simplicity, the robot arm is set as a square cylinder with the size of 100×100×1000 mm. It is actuated by external forces, which allows to generate complex deformations such as the compound deformation of elongation and twisting. Sixteen

planar electrodes are uniformly distributed on the surface of the manipulator to form the capacitive sensor array (4 layers and each consists of 4 electrodes). Each electrode is a 105×30 mm surface. The material parameters are set as Tab I. The results from this test case can be readily extended to a broader spectrum of manipulators with different sizes, shapes and actuation types.

TABLE I
MATERIAL PARAMETERS

Density	1.28×10^3 kg m^{-3}
Relative permittivity	3
Poisson's ratio	0.022
Young's modulus	4.15

We simulate three episodes of pseudo-continuous deformations with different external loads using solid mechanics and electrostatics CFS in COMSOL Multiphysics®. Each episode contains $n = 40$ discrete time frames. We compute the stationary solution in each time frame to mimic the continuous deformation by gradually increasing the magnitude of the external loads applied to the manipulator. We focus on the relationships between sensor signals and deformations in quasi-static conditions rather than in actual dynamics. This significantly simplifies the construction of simulation models and minimizes computational effort without affecting sensor characterization.

The first episode models a bending deformation (see Fig. 4), which is achieved by applying a force load in the x-y plane to the bottom of the structure, regarded here as the end-effector of the manipulator. The top is computationally treated as a fixed boundary and physically regarded as the base frame of the robotic artefact (the same settings are also adopted in the following episodes). The increase rate for the force is $(-0.613, -3.953, 0)$, i.e., the force in time frame t is $(-0.613t, -3.953t, 0)$ N. Note that the increase rate is generated randomly and we can modify its value to produce different bending deformations.

The second episode includes 2 stages (see Fig. 6). During the first stage (the first 13 time frames), the manipulator is twisted with the axis of $(-0.194, 0.004, -1)$. The increase rate for the twisting angle is -6.846, i.e., the twisting in time frame t is $-6.846t^\circ$. During the second stage, a force load with the increase rate of $(-1.667, 3.636, 0)$ is added, i.e., the force in time frame t is $(-1.667(t-13), 3.636(t-13), 0)$ N, while the twisting component remains constant.

The third episode models the compound deformation of twisting and elongation (see Fig. 7), which is achieved by simultaneously applying a rotation and a displacement along the z-axis to the bottom of the manipulator. The rotation axis is $(0.048, -0.069. -1)$. The increase rates for the rotation angle and the displacement are -2 and $(0, 0, -6)$, i.e., the rotation angle and displacement in time frame t are $-2t^\circ$ and $(0, 0, -6t)$ mm respectively.

From the measurement perspective, any two electrodes can form a capacitor and generate a capacitance readout. The 16-electrode capacitive sensor can theoretically produce 120 readouts per measurement frame. However, many of them are too small to be robustly measured in the physical world. To better approximate the practical conditions, we only record the capacitance readouts generated by two electrodes in the same layer and discard the others. Each layer includes 4 electrodes and can form 6 valid independent capacitance readouts per frame. In total, the 16-electrode sensor has 24 readouts per frame.

B. Case 2: pneumatic actuator

The second case models a simplified silicone-based pneumatic actuator with single chamber (see Fig. 3). The size of the actuator is 60×20×130 mm. The diameter of the flow inlet is 6 mm. Eight planar electrodes are uniformly placed on the surface of the actuator (2 layers and each contains 4 electrodes). Each electrode is a 16×50 mm flat surface. Using the measurement strategy in the first case, the sensor can produce 12 capacitance readouts per measurement frame.

Actuation is driven by prescribing an air inflow at the inlet boundary, which in turn drives the chamber deformation and is ultimately recorded via the capacitance measurements. This process is achieved by coupling laminar flow, mechanic and electrostatic fields through the method described in Section II. The simulation consists of 20 discrete time frames. The interval between two adjacent frames is 0.1 s. For the laminar flow field, the simulation parameters are set ad Tab II. We suppress backflow to ensure the air does not leave the chamber. Each inner surface is selected as the wall, and the no-slip condition is adopted. The speed of the air entering the pipe is constant at 0.7 m/s. A constant reference pressure point (0 Pa) is placed on the centre of the tail surface to ensure convergence and accelerate computation.

TABLE II
SIMULATION PARAMETERS

System temperature	293.15 K
System pressure	101.325 kPa
Dynamic viscosity of air	1.81e-5 kg/ms
Density of air	1.293 kg m^{-3}

The solid part of the actuator is modelled as a hyperelastic material with a wall thickness $d_t = 3$ mm. The Ogden model [18] is chosen as the silicone's model with bulk modulus $K =$ 4.157e4 MPa. The density of the silicone is $\rho_s = 1000$ kg m^{-3}. The relative permittivity of the silicone is taken as $\varepsilon_s = 3$, and that of air is $\varepsilon_a = 1$.

IV. RESULTS AND DISCUSSION

A. Capacitance readouts of the robot arm

The 24 capacitance readouts of the soft arm under the bending deformation over time is shown in Fig. 4. The calibrated capacitance is obtained using:

$$c = \frac{c_{\text{raw}} - c_{\text{nol}}}{c_{\text{nol}}} \tag{5}$$

where c is the calibrated capacitance; c_{raw} is the raw measurement and c_{nol} is the measurement without any loads. The signals from the capacitive sensor array change with the

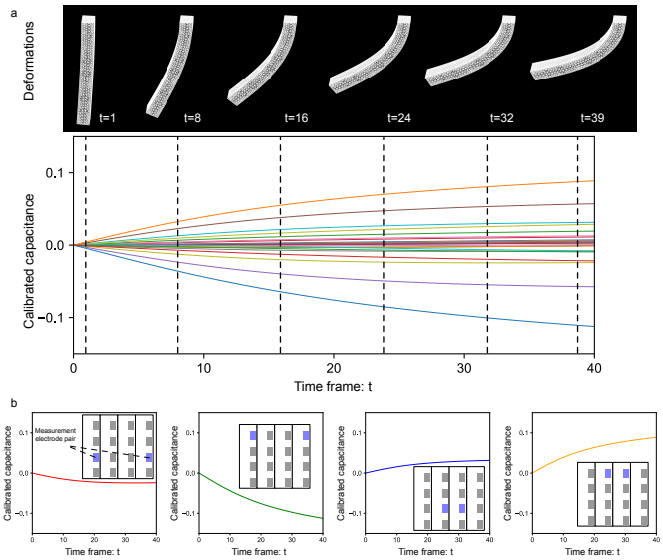

Fig. 4. Calibrated capacitance curves over time under the bending deformation. a, Examples of deformations in several selected frames and the calibrated capacitance readouts for all electrode pairs. b, The calibrated capacitance readouts for 4 selected electrode pairs.

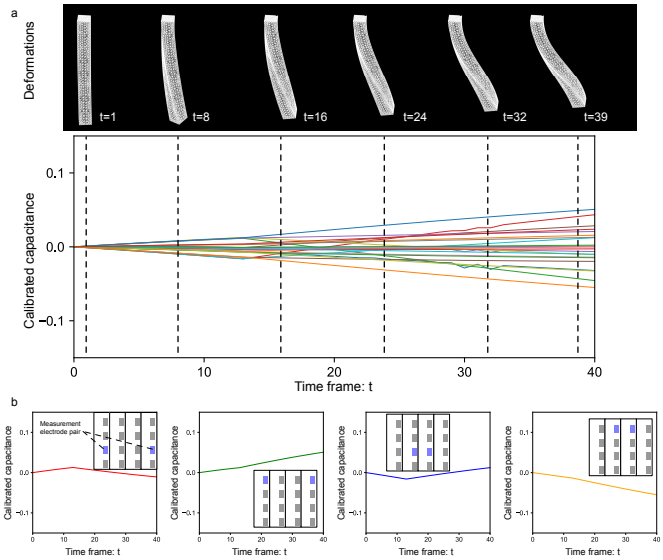

Fig. 6. Calibrated capacitance curves over time under the 2-stage twisting and bending deformation. a, Examples of deformations in several selected frames and the calibrated capacitance readouts for all electrode pairs. b, The calibrated capacitance readouts for 4 selected electrode pairs.

deformation, demonstrating the feasibility of applying it to soft robot perception.

Fig. 4 also shows that some capacitance readouts increase as the amplitude of the bending grows, while others have the opposite trend. This is because bending deformation causes one part of the soft body to expand (electrodes deployed in the area will also expand) while the other part contracts (electrodes deployed in the area will also contract). The locations of expansion and contraction depend on the bending direction. Fig. 5 shows the calibrated capacitance readout of the same electrode pair exhibits distinct responses to bending deformations in different directions. This property enables the proposed capacitive sensor array to measure bending direction.

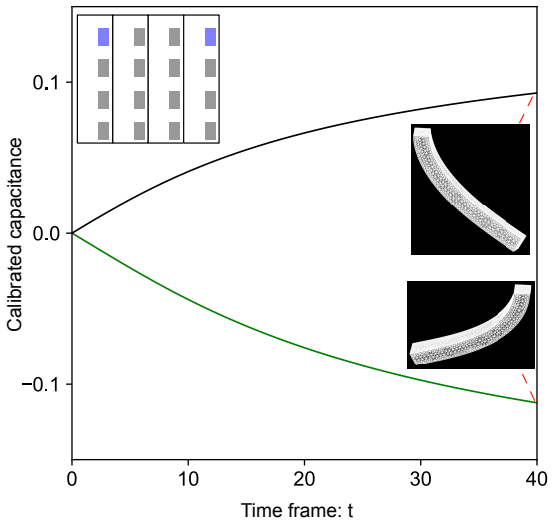

Fig. 5. Calibrated capacitance curves over time of bending deformations in two different directions.

Capacitance readouts of the 2-stage twisting and bending deformation are illustrated in Fig. 6. During the first stage (the first 13 time frames), pure twisting is implemented. The magnitude of the sensor response to twisting is smaller compared with that of bending, which results in the bending deformation dominating the capacitance readouts at the second stage. We can observe the flipping of several capacitance signals at the 14^{th} time frame due to the introduction of bending.

Fig. 7 shows the results of the compound deformation of elongation and twisting. The capacitance readouts monotonically increase with the degree of deformation. This is readily justified by the elongation deformation dominating the response of the capacitive sensor. The area of individual planar electrodes grows during elongation, leading to the increase in capacitance readouts.

B. Capacitance readouts of the pneumatic actuator

The results of the pneumatic actuator simulation are shown in Fig. 8. The capacitance readouts grow with the manipulator inflates if capacitors are formed by electrodes from the same surface, and the capacitance readouts decrease with the manipulator inflates if capacitors are formed by electrodes from different surfaces (see Fig. 8b). The increase of the capacitance readouts generated by the same surface electrode pairs is mainly caused by the area expansion of electrodes during manipulator inflation. The distance extension between electrodes in the inflation process makes the main contribution to the decrease of the capacitance readouts generated by different surface electrode pairs.

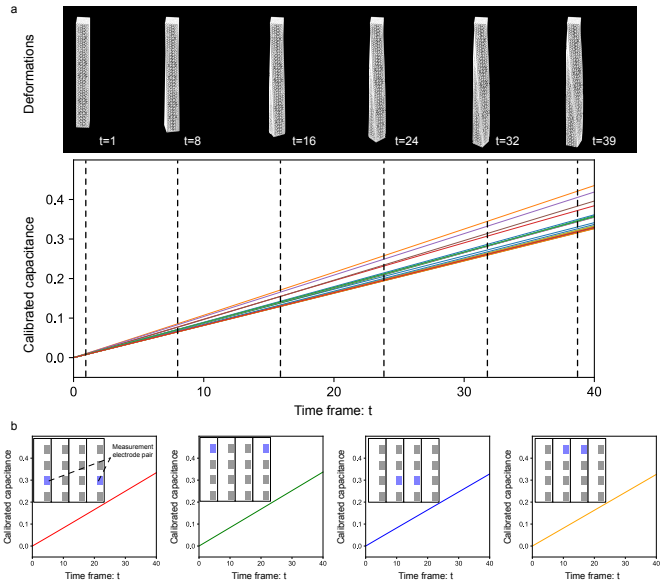

Fig. 7. Calibrated capacitance curves over time under the compound deformation of elongation and bending. a, Examples of deformations in several selected frames and the calibrated capacitance readouts for all electrode pairs. b, The calibrated capacitance readouts for 4 selected electrode pairs.

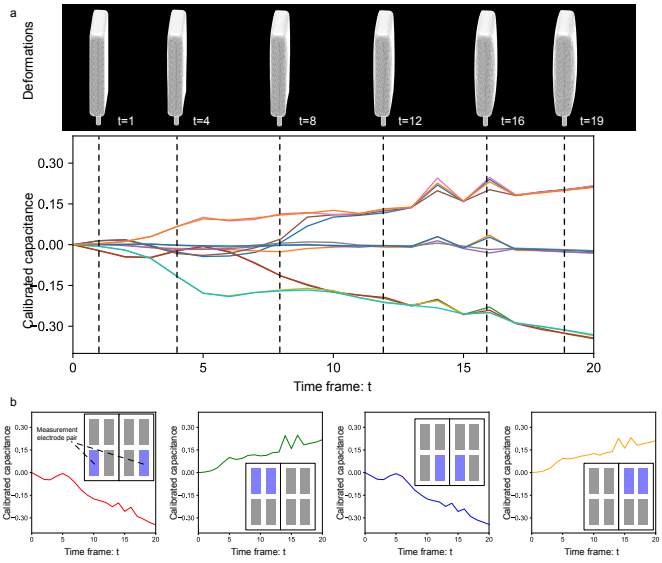

Fig. 8. Calibrated capacitance curves over time under the inflation deformation. a, Examples of deformations in several selected frames and the calibrated capacitance readouts for all electrode pairs. b, The calibrated capacitance readouts for 4 selected electrode pairs.

C. Perception tasks

The proposed CFS models that can seamlessly integrate robot dynamics and sensor response can generate a large number of annotated data, providing samples to train neural networks for various perception tasks. The networks trained with simulated data have the potential to be transferred to practical applications using sim-to-real transfer learning approaches, reducing the burden of data acquisition in the physical world. This subsection implements two typical perception tasks (i.e., applied force estimation and deformation classification) as case studies to demonstrate the potential of CFS.

Task 1: applied force estimation

Deformation induced by applied force can lead to the change of capacitance measurements, thus making it feasible to estimate the magnitude of force through capacitance readouts. We implement the CFS model for the soft manipulator subject to pure bending (which is presented in Section III) to generate annotated data. The bending deformation is induced by a force load $\boldsymbol{f} = (v_x t, v_y t, 0)$ applied to the tip of the manipulator. The parameters v_x and v_y are varied in each episode to ensure the diversity of the synthesis dataset. In total, we generate 300 episodes of data (12,000 time frames; with each episode containing 40 frames).

Our goal here is not to develop a novel algorithm with superiority for applied force estimation. Instead, we aim to verify the potential of CFS as a tool to analyze sensor and algorithm performance at the design stage. Therefore, we employ a simple multi-layer perceptron (MLP) [19] as the force estimator. The MLP has one hidden layer with 128 neurons. The input of the MLP is the 24-dimensional measurement vector from the capacitive sensor. The output is the estimation of the 2-dimensional force vector, i.e., $(\hat{f}_x, \hat{f}_y)$ (the component in the z direction is 0). The activation functions for the hidden and output layers are ReLU and Linear, respectively. The data are randomly divided into three exclusive groups, i.e., the training set (172 episodes, 6,880 frames), the validation set (74 episodes, 2,960 frames) and the testing set (54 episodes, 2,160 frames). We implement the network on the PyTorch platform. We use the Mean Squared Error (MSE) between prediction and ground truth as the loss of the force estimator. The Adam [20] optimizer is employed to update the learnable parameters and minimize the loss. We set the initial learning rate as 0.0005, which decays every 15 epochs by a factor of 1.2. The gradient is clipped with the threshold of 0.5. We train the network with the training set for 200 epochs and the batch size is set to 256. After training, the network with the least validation loss is retained as the final model. Two error metrics are employed here to quantitatively evaluate the performance of the trained network, i.e., Mean Square Error (MSE) and Mean Absolute Error (MAE), in this case, defined as:

$$\text{MSE} = \frac{1}{2N}\sum_{i=1}^{N}\left[(\hat{f}_x^i - f_x^i)^2 + (\hat{f}_y^i - f_y^i)^2\right] \tag{6}$$

$$\text{MAE} = \frac{1}{2N}\sum_{i=1}^{N}\left(|\hat{f}_x^i - f_x^i| + |\hat{f}_y^i - f_y^i|\right) \tag{7}$$

where N is the number of samples and superscript i represents the i-th sample.

The trained MLP can achieve 1.373 for MAE and 3.589 for MSE on the testing set. The estimation results for f_x and f_y on the testing set are shown in Fig.9. We observe that samples distributed in the middle have smaller errors. A likely explanation for this lies with the unbalanced distribution of training samples and the limited expressive power of the MLP when associated with only one hidden layer. Fig.10 shows two examples of the ground truth deformations, the corresponding applied force and the estimation of the MLP.

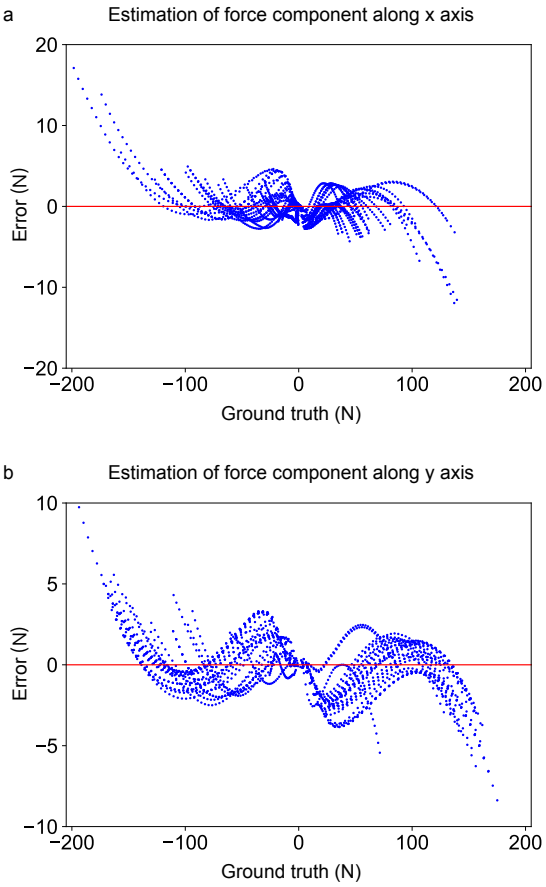

Fig. 9. Absolute error for force estimation on the testing set. a, absolute error for force component along x axis. b, absolute error for force component along y axis.

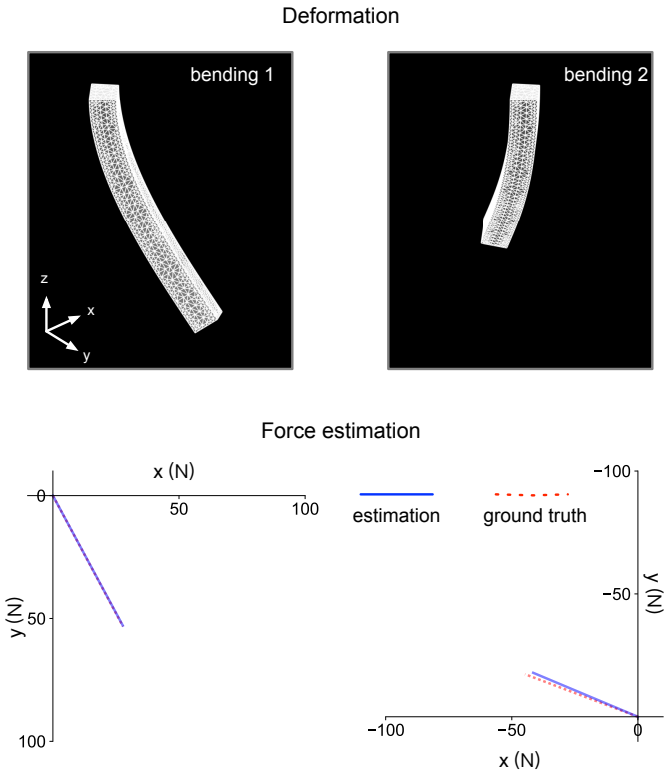

Fig. 10. Examples of force estimation on the testing set. Top: the ground truth deformations. Bottom: the ground truth applied force (red dot line) and the estimated force (blue line).

Task 2: deformation classification

The capacitance signals induced by different types of deformations have distinct patterns. This property enables the proposed sensor array to be applied to classify deformations. We attempt to train a binary classifier which can tell the difference between pure bending (the first type of deformations described in Section III) and 2-stage twisting and bending deformation (the second type of deformations described in Section III). We already obtain 300 episodes of pure bending data in task I. We implement the CSF model presented in Section III to generate 298 episodes of data for 2-stage twisting and bending deformation. The diversity of the synthesis dataset is ensured by varying the values of external loads including the axis of twisting, the increase rate for twisting angle and the increase rate for the applied force. Complementary with the dataset produced for the force estimation task, we totally have 598 episodes of data.

We set the class label of pure bending as 0 and 2-stage twisting and bending deformation as 1. We only retain the data after the 14^{th} frame in each episode to ensure the difference between deformations is sufficiently large to be detected. Finally, we construct a dataset with 15,548 frames of samples, among which 7,748 frames belong to deformation 1 (the combination of bending and twisting) and the remaining 7,800 frames are deformation 0 (pure bending).

We select an MLP with one hidden layer as the classifier. Its structure is the same as the force estimator except for the dimension (1) and the activation function (Sigmoid) of the output layer. We feed the capacitance vector to the MLP classifier and expect it to output the prediction of the class label (i.e., the probability that the deformation contains a twisting). The data are randomly divided into three exclusive groups, i.e., the training set (343 episodes, 8,918 frames), the validation set (147 episodes, 3,822 frames) and the testing set (108 episodes, 2,808 frames). We select the binary cross entropy loss function and train the classifier using the same training procedure (the only difference is that we set the initial learning rate as 0.0001). After training, the classifier can achieve 100% classification accuracy on the testing set, which demonstrates the feasibility of using capacitance signals to distinguish these two types of deformations. Two examples of deformation classification are shown in Fig.11. Note that the 100% accuracy is only achievable under ideal circumstances. In this study, the classification task is very simple, which only includes 2 deformation classes, and the signals are assumed to be noise free. The accuracy is expected to drop if the task involves more types of deformations and/or the noise is taken into account.

V. Conclusions

We developed CFS models for capacitive sensor arrays on two types of soft manipulators. The CFS models can seamlessly integrate the sensing and mechanical components

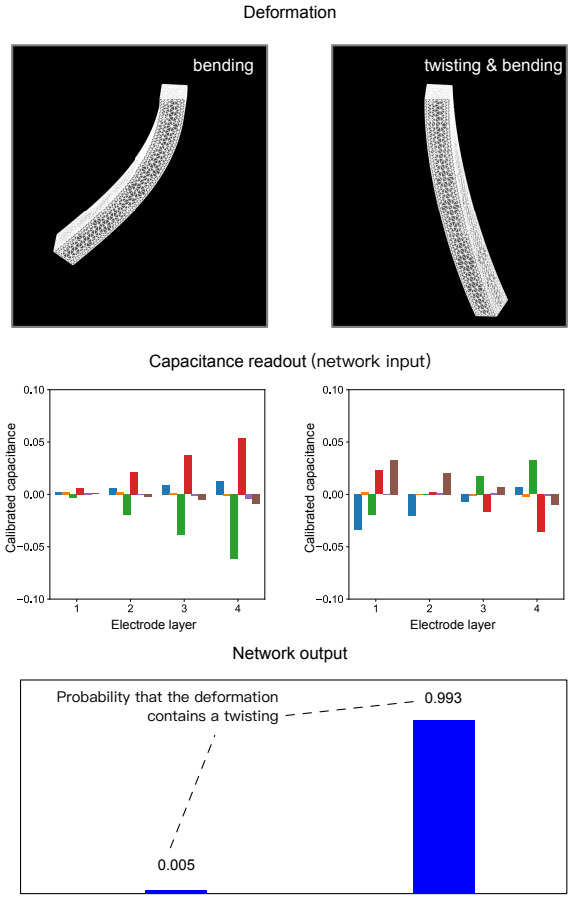

Fig. 11. Examples of deformation classification on the testing set. Top: the ground truth deformations. Middle: the corresponding measurements (the input of the MLP classifier). Bottom: the output of the MLP classifier.

of soft robots. We implemented the CFS models to characterize the capacitive sensor arrays in various deformations, which helped us better understand sensor behaviours. The case studies for two perception tasks (i.e., applied force estimation and deformation classification) based on the annotated dataset produced through CFS demonstrate the potential of CFS to benefit learning-based perception. Combined with simple machine learning frameworks, the capacitance sensor arrays perform well in both the applied force estimation task (1.373 MAE) and the deformation classification task (100% accuracy). The models trained with simulated data could be transferred to practical applications using sim-to-real transfer learning approaches, significantly reducing time and costs for data acquisition through physical experiment platforms.

REFERENCES

[1] M. R. Pedersen, L. Nalpantidis, R. S. Andersen, C. Schou, S. Bøgh, V. Krüger, and O. Madsen, "Robot skills for manufacturing: From concept to industrial deployment," *Robotics and Computer-Integrated Manufacturing*, vol. 37, pp. 282–291, 2016. [Online]. Available: https://www.sciencedirect.com/science/article/pii/S0736584515000575

[2] A. H. Reddy, B. Kalyan, and C. S. N. Murthy, "Mine rescue robot system –a review," *Procedia Earth and Planetary Science*, vol. 11, pp. 457–462, 2015. [Online]. Available: https://www.sciencedirect.com/science/article/pii/S187852201500096X

[3] D. Rus and M. T. Tolley, "Design, fabrication and control of soft robots," *Nature*, vol. 521, no. 7553, pp. 467–475, 2015. [Online]. Available: https://doi.org/10.1038/nature14543

[4] C. Laschi, B. Mazzolai, and M. Cianchetti, "Soft robotics: Technologies and systems pushing the boundaries of robot abilities," *Science Robotics*, vol. 1, no. 1, p. eaah3690, 2021/10/02 2016. [Online]. Available: https://doi.org/10.1126/scirobotics.aah3690

[5] E. Coevoet, T. Morales-Bieze, F. Largilliere, Z. Zhang, M. Thieffry, M. Sanz-Lopez, B. Carrez, D. Marchal, O. Goury, J. Dequidt, and C. Duriez, "Software toolkit for modeling, simulation, and control of soft robots," *Advanced Robotics*, vol. 31, no. 22, pp. 1208–1224, 11 2017. [Online]. Available: https://doi.org/10.1080/01691864.2017.1395362

[6] E. Coevoet, A. Escande, and C. Duriez, "Soft robots locomotion and manipulation control using fem simulation and quadratic programming," in *2019 2nd IEEE International Conference on Soft Robotics (RoboSoft)*, 2019, pp. 739–745.

[7] C. Armanini, M. Farman, M. Calisti, F. Giorgio-Serchi, C. Stefanini, and F. Renda, "Flagellate underwater robotics at macroscale: Design, modeling, and characterization," *IEEE Transactions on Robotics*, pp. 1–17, 2021.

[8] F. Renda, F. Giorgio-Serchi, F. Boyer, C. Laschi, J. Dias, and L. Seneviratne, "A unified multi-soft-body dynamic model for underwater soft robots," *The International Journal of Robotics Research*, vol. 37, no. 6, pp. 648–666, 2018.

[9] D. S. Shah, J. P. Powers, L. G. Tilton, S. Kriegman, J. Bongard, and R. Kramer-Bottiglio, "A soft robot that adapts to environments through shape change," *Nature Machine Intelligence*, vol. 3, no. 1, pp. 51–59, 2021. [Online]. Available: https://doi.org/10.1038/s42256-020-00263-1

[10] F. Corucci, N. Cheney, F. Giorgio-Serchi, J. Bongard, and C. Laschi, "Evolving soft locomotion in aquatic and terrestrial environments: Effects of material properties and environmental transitions," *Soft Robotics*, vol. 5, no. 4, pp. 475–495, 2021/10/03 2018. [Online]. Available: https://doi.org/10.1089/soro.2017.0055

[11] A. Spielberg, A. Amini, L. Chin, W. Matusik, and D. Rus, "Co-learning of task and sensor placement for soft robotics," *IEEE Robotics and Automation Letters*, vol. 6, no. 2, pp. 1208–1215, 2021.

[12] O. Goury and C. Duriez, "Fast, generic, and reliable control and simulation of soft robots using model order reduction," *IEEE Transactions on Robotics*, vol. 34, no. 6, pp. 1565–1576, 2018.

[13] W. Yang and L. Peng, "Image reconstruction algorithms for electrical capacitance tomography," *Measurement science and technology*, vol. 14, no. 1, p. R1, Image reconstruction algorithms for electrical capacitance tomography 2002.

[14] S. Wang, J. Ye, and Y. Yang, "Quantitative measurement of two-phase flow by electrical capacitance tomography based on 3d coupling field simulation," *IEEE Sensors Journal*, vol. 21, no. 18, pp. 20 136–20 144, 2021.

[15] C. L. Dym, I. H. Shames *et al.*, *Solid mechanics*. Springer, 1973.

[16] B. R. Munson, T. H. Okiishi, W. W. Huebsch, and A. P. Rothmayer, *Fluid mechanics*. Wiley Singapore, 2013.

[17] P. Breitman, Y. Matia, and A. D. Gat, "Fluid mechanics of pneumatic soft robots," *Soft Robotics*, 2021/10/11 2020. [Online]. Available: https://doi.org/10.1089/soro.2020.0037

[18] R. Ogden, "Non-linear elastic deformations," *Engineering Analysis*, vol. 1, no. 2, p. 119, 1984.

[19] I. Goodfellow, Y. Bengio, and A. Courville, *Deep learning*. MIT press, 2016.

[20] D. P. Kingma and J. Ba, "Adam: A method for stochastic optimization," in *International Conference on Learning Representations (ICLR)*, 2015.